Regional Deformation of the Optic Nerve Head and Peripapillary Sclera During IOP Elevation

Elias Pavlatos,[1] Yanhui Ma,[1] Keyton Clayson,[1,2] Xueliang Pan,[3] and Jun Liu[1,2,4]

[1]Department of Biomedical Engineering, Ohio State University, Columbus, Ohio, United States
[2]Biophysics Interdisciplinary Group, Ohio State University, Columbus, Ohio, United States
[3]Department of Biomedical Informatics, Ohio State University, Columbus, Ohio, United States
[4]Department of Ophthalmology and Visual Science, Ohio State University, Columbus, Ohio, United States

Correspondence: Jun Liu, Department of Biomedical Engineering, Ohio State University, 270 Bevis Hall, 1080 Carmack Road, Columbus, OH 43210, USA; liu.314@osu.edu.

Submitted: March 30, 2018
Accepted: June 30, 2018

Citation: Pavlatos E, Ma Y, Clayson K, Pan X, Liu J. Regional deformation of the optic nerve head and peripapillary sclera during IOP elevation. *Invest Ophthalmol Vis Sci*. 2018;59:3779–3788. https://doi.org/10.1167/iovs.18-24462

Purpose. To measure the deformation of the porcine optic nerve head (ONH) and peripapillary sclera (PPS) in response to intraocular pressure (IOP) elevation.

Methods. High-frequency ultrasound was used to image the ONH and PPS of 12 porcine eyes during ex vivo inflation testing from 5 to 30 mm Hg. A speckle tracking algorithm was used to compute tissue displacements in the anterior-posterior direction and expansion of the scleral canal. Through-thickness, in-plane, and shear strains were calculated within the ONH. Regional displacements and strains were analyzed and compared.

Results. The ONH and PPS showed overall posterior displacement in response to IOP elevation. Posterior displacement of the ONH was larger than and strongly correlated with the posterior displacement of the PPS throughout inflation testing. Scleral canal expansion was much smaller and leveled off quicker than ONH posterior displacement as IOP increased. Through-thickness compression was concentrated in the anterior ONH, which also experienced larger in-plane and shear strains than the posterior ONH. Within the anterior ONH, all three strains were significantly higher in the periphery compared with the center, with the shear strain exhibiting the greatest difference between the two regions.

Conclusions. High-resolution ultrasound speckle tracking revealed the full-thickness mechanical response of the posterior eye to IOP elevation. A mismatch in posterior displacement was found between the ONH and PPS, and regional analyses showed a concentration of strains within the periphery of the anterior porcine ONH. These deformation patterns may help in understanding IOP-associated optic nerve damage and glaucoma susceptibility.

Keywords: glaucoma, biomechanics, ultrasound, optic nerve head, peripapillary sclera

The axons of retinal ganglion cells are damaged in glaucoma, resulting in progressive and irreversible vision loss. The optic nerve head (ONH) has been a focus in glaucoma research, as this region was shown to exhibit the earliest signs of axonal damage.[1] At the ONH, the axons converge into bundles to pass through the pores of the cribriform lamina cribrosa (LC), which spans the scleral canal and is continuous with the adjacent peripapillary sclera (PPS).[2] The LC and PPS are the primary load-bearing structures of the posterior eye that provide structural and functional support to the axons.

One of the main risk factors for developing glaucoma is elevated intraocular pressure (IOP). Increases in IOP cause increased stresses and strains within the ONH and PPS and these mechanical insults may directly impact axonal function or impair blood flow by compressing, stretching, or shearing the blood vessels or LC beams.[3,4] Evidence has also shown that astrocytes within the ONH are mechanosensitive,[5] and their responses to increased mechanical loading may result in reduced trophic support to axons or detrimental extracellular matrix remodeling.[6] Determining the role of these potential mechanisms requires a thorough understanding of the mechanical environment experienced by the cells and tissues in this region. It is therefore important to measure the deformation of the tissues within and around the ONH in response to IOP elevation.

A number of imaging methods have been used to study the IOP-related deformation of the ONH. Optical coherence tomography (OCT) and second harmonic-generated imaging have emerged as valuable tools for high-resolution measurement of ONH deformation, but penetration depth is limited to the superficial couple hundreds of microns.[7,8] Phase-contrast microcomputed tomography (PC-μCT) can achieve better penetration depth but may not be cost effective for a large sample size.[9] These previous studies have also focused primarily on the ONH and have not analyzed the relationship between the ONH and the surrounding PPS in the same eye, which will likely provide a more complete understanding of ONH biomechanics.[10,11]

Our laboratory has developed 2D and 3D high-frequency ultrasound speckle tracking methods and used them to measure IOP-induced deformation of the cornea and posterior sclera.[4,12–14] High-frequency ultrasound achieves a balance between resolution and penetration depth, enabling accurate measurement of small deformations and full-thickness imaging of both the ONH and PPS simultaneously. In this study, we used our ultrasound speckle tracking technique to measure displace-

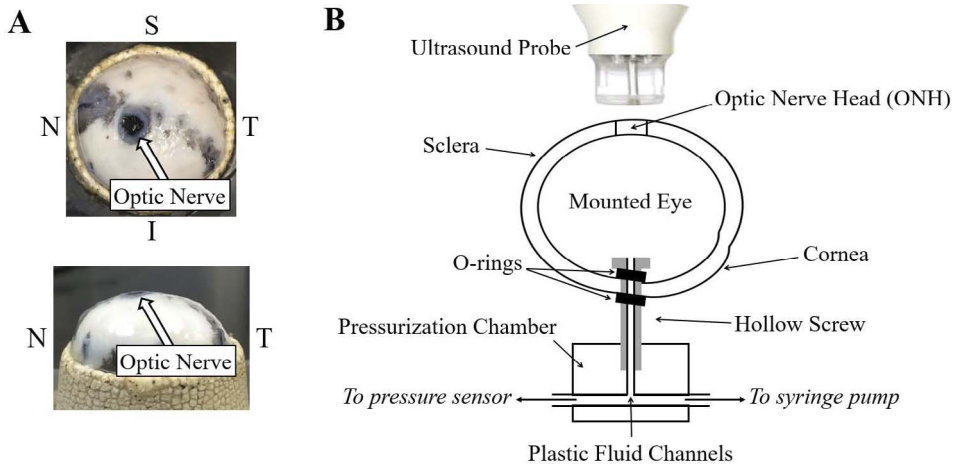

Figure 1. (**A**) Photos of a porcine eye showing the optic nerve trimmed to be flush with the PPS. (**B**) Experimental setup used for inflation testing. The ultrasound probe was aligned along the nasal-temporal meridian of the globe.

ments and strains within the porcine ONH and PPS during controlled IOP elevation. The goals of the study were to quantify and map the mechanical behavior of the ONH and PPS throughout the entire thickness of the tissues and to evaluate regional variability in their responses to elevated IOP.

Methods

Sample Preparation

Twelve porcine globes from animals between 4 and 6 months old were obtained from a United States Department of Agriculture-approved abattoir under Hazard Analysis and Critical Control Points guidelines (SiouxPreme Packing Co., Sioux City, IA, USA). The globes were immersed in saline and kept cold during shipping, and all eyes were tested within 72 hours postmortem. The extraocular tissues were trimmed away, and the optic nerve was cut to be flush with the outer surface of the PPS (Fig. 1A). Eyes were mounted on a customized pressurization chamber to undergo inflation testing (Fig. 1B). A small portion of the anterior globe opposite to the ONH, consisting mostly of corneal tissue and a small amount of anterior sclera, was removed using a 7.5-mm trephine. The lens and vitreous were removed and the head of a hollow plastic mounting screw was inserted into the eye via the trephined hole. Two O-rings, one on either side of the ocular shell, were used to facilitate a fluid-tight seal. A small amount of cyanoacrylate glue was placed around the outer O-ring to ensure the integrity of the seal. The mounting screw was then wrapped with polytetrafluoroethylene tape and inserted into the pressurization chamber.

Inflation Testing

The eye and pressurization chamber were immersed in 0.9% saline. The chamber contained fluid channels that connected the end of the mounting screw to a programmable syringe pump (PHD Ultra, Harvard Apparatus, Holliston, MA, USA) and a pressure sensor (P75, Harvard Apparatus) to continuously control and monitor IOP. Each globe was preconditioned using 20 pressure cycles from 5 to 30 mm Hg, followed by an equilibration period of 30 minutes at 5 mm Hg. Inflation testing was then performed by increasing IOP from 5 to 30 mm Hg, with pressure steps of 0.5 mm Hg. A 55-MHz ultrasound probe (Vevo 660, VisualSonics Inc., Toronto, Canada) was positioned along the nasal-temporal meridian of the eye (Fig. 1B). After a 15-second delay at each IOP step, a 2D image of the ONH and PPS was obtained at a frame rate of ~10 frames/sec before increasing IOP to the next pressure level. IOP control and data acquisition were implemented using a customized LabView interface (National Instruments, Austin, TX, USA).

Ultrasound Speckle Tracking

The 2D ultrasound speckle tracking technique used in this study has been validated previously.[12] Speckle tracking is performed using the radiofrequency data from each ultrasound image. The radiofrequency data are sampled discretely to generate pixels, and the sampling rate determines the distance between pixels. The pixel height is 1.5 μm in the vertical direction (i.e., the direction of ultrasound propagation and anterior-posterior direction anatomically), and the pixel width is 20.8 μm in the horizontal direction (i.e., the direction perpendicular to the direction of ultrasound propagation and nasal-temporal direction anatomically).

The first step in the speckle tracking algorithm is to divide the tissue into a grid of rectangular kernels, each containing roughly 1500 pixels. The kernel dimensions are 76.5 μm × 644.8 μm (vertical × horizontal), and the kernels are overlapped by 50%. Previous studies have shown that overlapping kernels by 50% results in the best combination of strain spatial resolution and strain signal-to-noise ratio.[12] Each kernel is tracked individually between images acquired at different IOP levels, and cross-correlation is used to find the new kernel location. The vertical and horizontal components of the displacement vector are calculated with respect to the kernel locations at the initial IOP level (i.e., 5 mm Hg). The displacement of kernels with a correlation coefficient below 0.8 or with a displacement that differs by more than two standard deviations from the average displacement in the 5 × 5 neighborhood of the kernel is replaced by the neighborhood average to reduce noise in the displacement field. 2D least squares strain estimation is used to calculate the vertical and horizontal strains for each kernel based on the 5 × 5 neighborhood of kernels.[15] A coordinate transformation converts the strains from the vertical and horizontal directions to the through-thickness (perpendicular to the tissue curvature) and in-plane (parallel to the tissue curvature) directions (Fig. 2A):

Investigative Ophthalmology & Visual Science

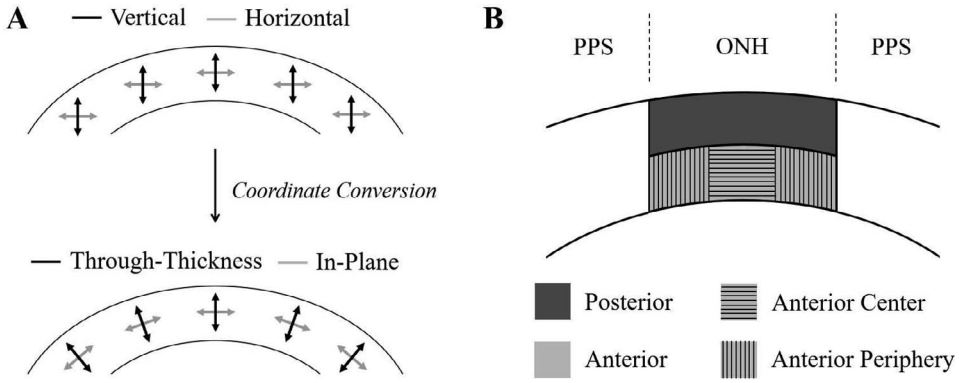

Figure 2. **(A)** Orientation of the through-thickness and in-plane strains after conversion from the vertical and horizontal directions. **(B)** Divisions of the ONH used in the regional analysis of strain.

$$\begin{bmatrix} \varepsilon_{\varphi} & \varepsilon_{\varphi r} \\ \varepsilon_{\varphi r} & \varepsilon_{r} \end{bmatrix} = \begin{bmatrix} \cos\theta & \sin\theta \\ -\sin\theta & \cos\theta \end{bmatrix} \begin{bmatrix} \varepsilon_{x} & \varepsilon_{xy} \\ \varepsilon_{xy} & \varepsilon_{y} \end{bmatrix} \begin{bmatrix} \cos\theta & -\sin\theta \\ \sin\theta & \cos\theta \end{bmatrix} \quad (1)$$

where ε_x and ε_y are the horizontal and vertical strains, ε_r and ε_φ are the through-thickness and in-plane strains, and θ is the angle between the two coordinate systems. θ is calculated from the coordinates of the kernel and those of the center of the sphere fit to the contours of the ONH and PPS. The remaining strain variables represent the shear components, and the magnitudes (absolute values) were used for quantitative analyses.

Segmentation and Regional Analyses

After speckle tracking and displacement calculations, the kernels were manually segmented into those that belonged to the ONH and those that belonged to the PPS. The boundaries between the ONH and PPS were determined using the B-mode ultrasound images, because the sclera is much brighter than the ONH in ultrasound images. The boundaries between the ONH and PPS were selected to be the location where the bright signal from the sclera abruptly ended when moving from the edge of the image toward the ONH. The kernels between the left and right boundaries were used for calculating the average ONH displacements and strains, and the kernels outside of the boundaries were assigned to the PPS. It is noted that the subjective selection of the boundary line was performed using the B-mode image (i.e., at the pixel level). Although the interobserver difference in selecting the boundary could be up to 5 pixels according to our experiences, our results showed that the segmentation of kernels was minimally affected because the kernels were larger in size and their locations were determined prior to segmentation.

Expansion of the scleral canal was calculated as the difference in the average horizontal displacement between the PPS on either side of the ONH. The strains were compared for the anterior and posterior ONH and for the central and peripheral regions of the anterior ONH (Fig. 2B). The inner and outer boundaries of the ONH were fit by two concentric circles, and the average radius of the inner and outer fits was used to split the kernels within the ONH into equal-thickness anterior and posterior halves (Fig. 3B). The kernels in the anterior ONH were further segmented into central and peripheral regions by dividing them into equal horizontal thirds. The average strain in the central region of the anterior ONH was calculated from the strain values of the kernels in the middle third, and the average strain in the periphery was calculated using the strain values of the kernels in the peripheral two thirds. Strains were not calculated for all edge kernels, which did not have a full 5×5 neighborhood of kernels.

The differences in displacement or strain between different regions were evaluated at each IOP level by using paired *t*-tests. The reported *P* values were computed without multiple comparison corrections. The conclusion of significant difference between regions was based on all tests at different pressure levels, with the Hochberg's step-up method controlling family-wise error rate of 0.05.[16] Hochberg's step-up method declares that all tests are significant if the highest *P* value of these tests is less than 0.05, which is more powerful than the Bonferroni method or the Holms procedure for multiple comparison adjustment. As a sensitivity analysis, linear mixed models for repeated measures (at selected IOP levels and different regions for each eye) were used to confirm

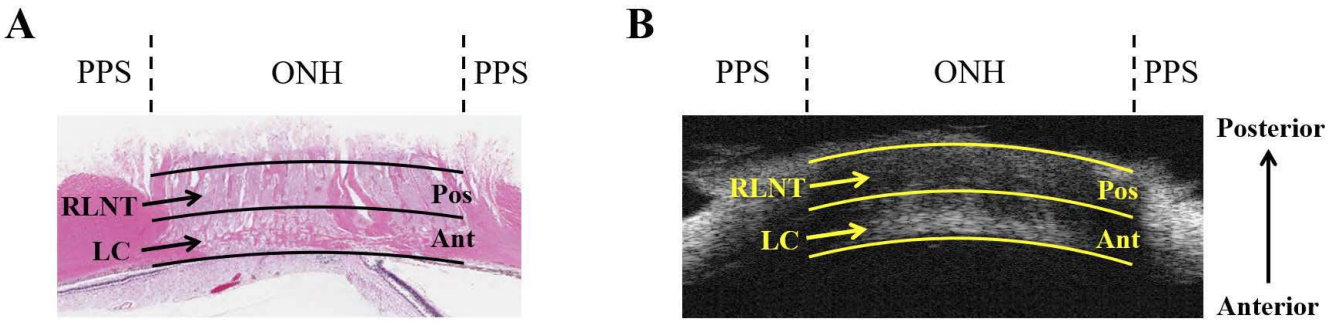

Figure 3. **(A)** Histology image and **(B)** ultrasound image of a porcine eye at 30 mm Hg. The LC can be seen in the anterior ONH in both images. RLNT, retrolaminar neural tissue; Ant, anterior; Pos, posterior.

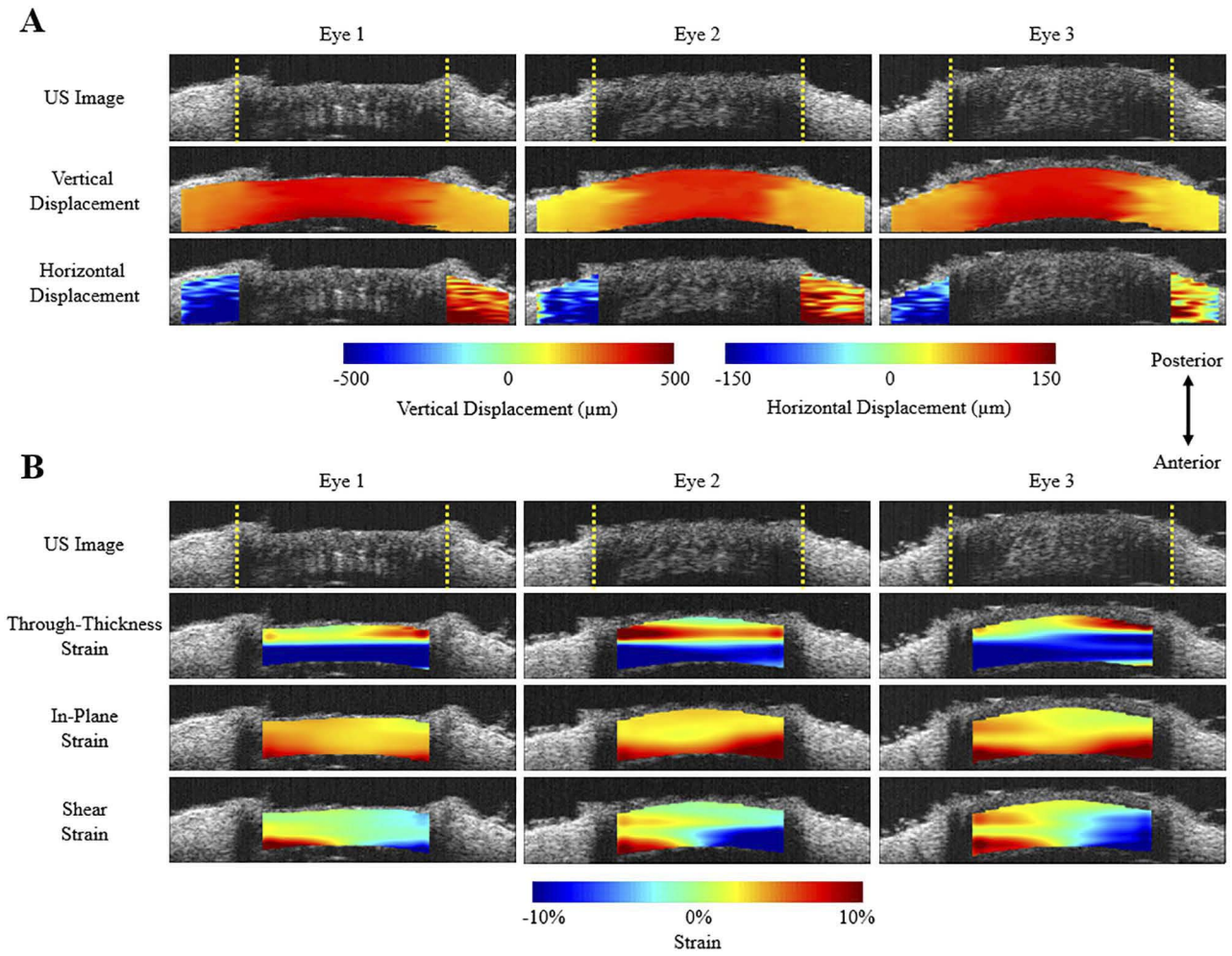

Figure 4. (**A**) Displacement maps for three porcine eyes at 30 mm Hg. Positive displacements correspond to posterior vertical movement or rightward horizontal movement (the *color bar* is adjusted for each direction). The ONH had a larger vertical (posterior) displacement than PPS. The horizontal displacement was negative (*blue*) in the left PPS and positive (*red*) in the right PPS, indicating canal expansion. The horizontal displacements of the ONH were not included in the calculation of canal expansion and are not shown. (**B**) Strain maps for the same three eyes at 30 mm Hg. Large compressive through-thickness strains were mostly in the anterior ONH, whereas the in-plane and shear strains were largely concentrated in the periphery of the anterior ONH. The shear strains were opposite in sign for the left and right sides of the ONH, indicating posterior bending. The *yellow dashed lines* in the ultrasound images show the separation of the ONH and PPS. The strains within the PPS were not calculated. The maps were generated after interpolation and smoothing of the kernel displacements and strains.

the overall differences between regions. In addition, the Pearson correlation coefficients of the measures of different regions were evaluated at each pressure level.

Histology

Histologic analyses were performed to identify the structures that were present in each region of the porcine ONH and PPS. Three eyes were immersed in a 10% formalin solution for 24 hours following the inflation testing. A tissue section was prepared from each eye along the nasal-temporal meridian, corresponding approximately to the cross-section imaged using ultrasound. The sections were stained using hematoxylin and eosin and compared with the ultrasound images to confirm the location of corresponding anatomic structures.

Results

Histology images revealed the LC spanning the width of the scleral canal, with its insertion points located near the anterior boundary of the PPS (Fig. 3). This LC location is consistent with previous reports in porcine eyes,[9,17–19] and corresponded to a region of higher echogenicity within the ONH in the ultrasound images. A division of the ONH into anterior and posterior halves showed the LC present within the anterior half of the ONH in both the ultrasound and histology images. The posterior layer appeared to be composed primarily of the retrolaminar neural tissue.

The ONH and PPS were both displaced posteriorly during IOP elevation in all 12 eyes. The relationship between IOP and posterior displacement was nonlinear. The ONH had consistently larger posterior displacement than the PPS at all IOP levels ($P < 0.001$; Figs. 4A, 5A). At the peak IOP of 30 mm Hg, displacement of the ONH was 348.9 ± 82.2 μm (mean ± SD) ranging from 213.1 to 514.9 μm, and displacement of the PPS was 219.7 ± 65.8 μm (mean ± SD) ranging from 131.4 to 351.5 μm. The average difference between ONH and PPS posterior displacement was 129.2 ± 24.7 μm. Although there was a substantial difference in magnitude, a strong positive correlation was found between the posterior displacement of the ONH and PPS ($R > 0.96$, for all IOP levels; Fig. 5B).

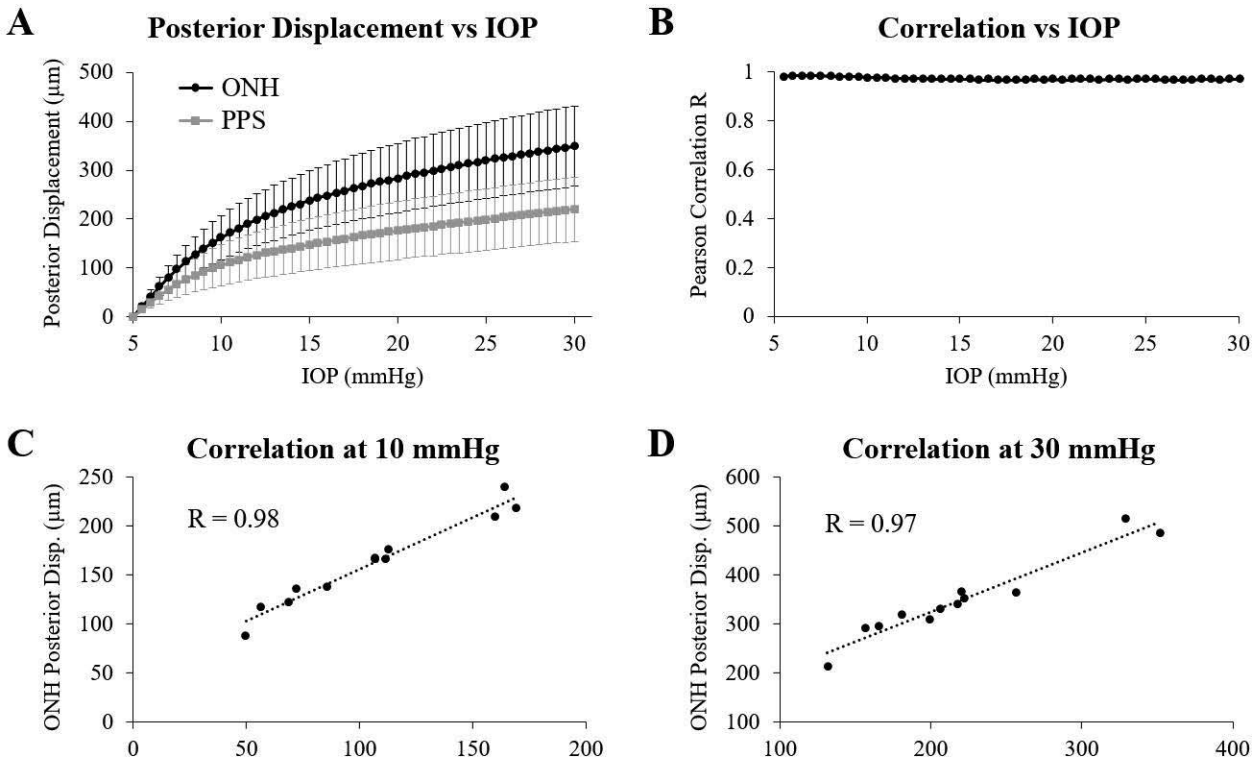

Figure 5. (**A**) Average posterior displacement of the ONH and PPS during inflation ($n = 12$). (**B**) Pearson correlation between ONH and PPS posterior displacement at all IOP levels. Scatterplots of ONH and PPS posterior displacement are shown in (**C**) and (**D**) at 10 and 30 mm Hg, respectively.

Expansion of the scleral canal also exhibited a nonlinear increase during inflation, leveling off quickly after IOP reached about 10 mm Hg (Fig. 6A). The average expansion was 127.7 ± 31.3 µm (min, 76.6 µm; max, 163.5 µm) at 30 mm Hg. The posterior displacement of the ONH was greater in magnitude than the expansion of the scleral canal throughout the inflation test ($P < 0.001$ for all IOP levels; Figs. 4A, 6A). The ONH posterior displacement and canal expansion were correlated at lower levels of IOP, with a larger posterior displacement associated with more canal expansion. However, the correlation weakened with increasing IOP (Figs. 6B–D).

The strains within the ONH showed nonlinear increases during IOP elevation (Fig. 7A). In all eyes, the strains exhibited substantial depth-dependent variability (Fig. 4B). The magnitudes of all three strains were significantly higher in the anterior ONH compared with the posterior ONH ($P < 0.001$ at all IOP levels for each type of strain; Fig. 7A). The largest measured deformation at 30 mm Hg was through-thickness compression of the anterior ONH (Table 1). In the posterior ONH, some eyes showed through-thickness compression, whereas others exhibited through-thickness expansion, causing the average across the 12 eyes to be close to zero. In both the anterior and posterior ONH, the through-thickness strain was significantly larger than the in-plane and shear strains ($P \leq 0.003$ for both comparisons at all IOP levels). The in-plane strains in the anterior and posterior ONH were positively correlated at every IOP level (all but one $R > 0.75$; Fig. 7B). The anterior and posterior shear strain magnitudes were correlated with $R > 0.6$ at levels up to 19 mm Hg, but the correlation steadily decreased at higher IOP levels (Fig. 7B). The through-thickness strains for the two regions were correlated with $R > 0.6$ only at a few IOP levels below 9 mm Hg.

In the anterior ONH, the largest deformations were concentrated at the periphery (Fig. 4B). Both the in-plane stretch and shear strain were significantly higher in the periphery than the center throughout the inflation ($P < 0.02$ for all IOP steps; Fig. 8A). At 30 mm Hg, the in-plane stretch and shear strains were approximately 2 times higher in the periphery compared with the center, whereas the through-thickness compression was about 1.2 times higher (Table 2). The through-thickness compression was consistently larger than the in-plane stretch and shear strain in both the center and periphery ($P < 0.002$ for all IOP steps). A correlation between the central and peripheral regions was found at all IOP levels for the through-thickness compression and at all IOP levels except 5.5 mm Hg for the in-plane stretch (all $R > 0.8$; Fig. 8B). The shear strains were also correlated between the two regions for the majority of the IOP steps (all $R > 0.6$).

Discussion

To the best of our knowledge, this is the first study to simultaneously measure the mechanical behavior of both the ONH and PPS in the porcine eye, which has a collagenous LC structure similar to that of the human eye. The primary findings include the following:

- During an acute IOP increase, both the ONH and PPS were displaced posteriorly, the ONH exhibited a significantly larger posterior displacement than the PPS, and the displacements of the two regions were strongly correlated.
- The expansion of the scleral canal was much smaller in magnitude than the posterior displacement of the ONH, and the correlation between canal expansion and ONH posterior displacement decreased as IOP increased from

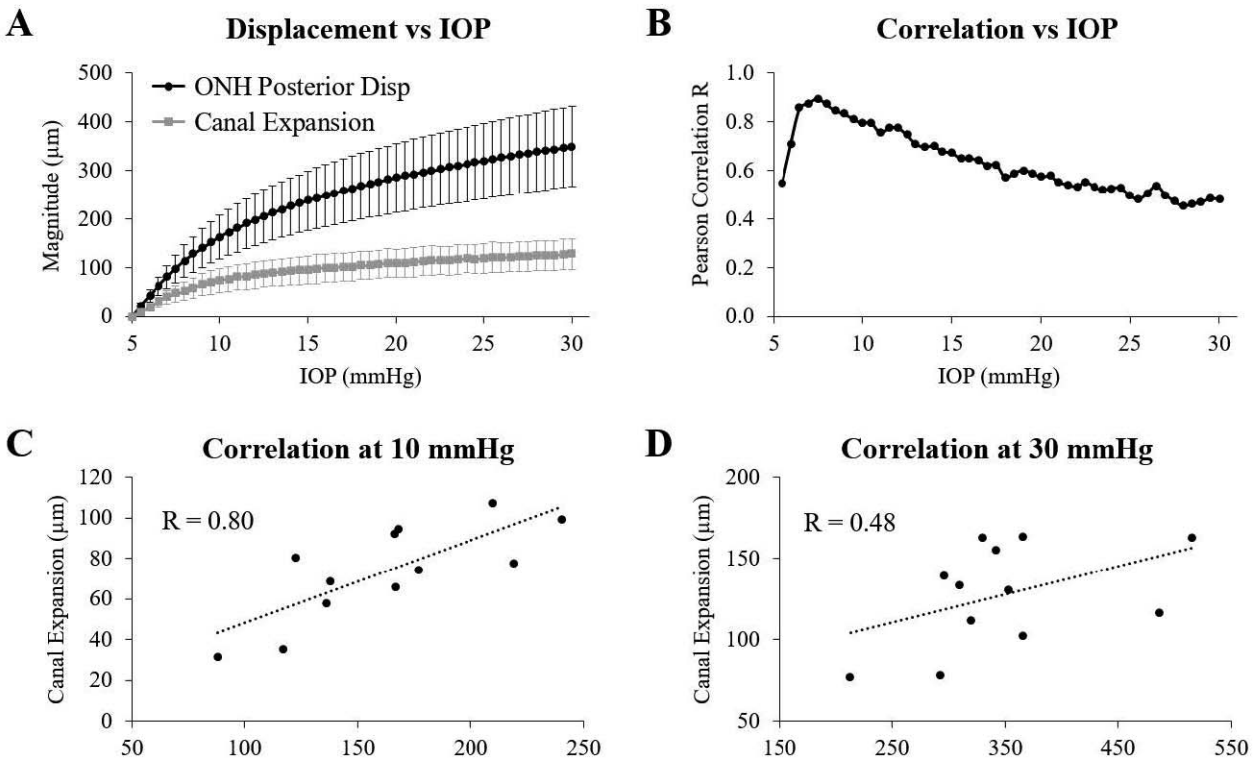

Figure 6. (**A**) Average ONH posterior displacement and scleral canal expansion during inflation ($n = 12$). (**B**) Pearson correlation between ONH posterior displacement and scleral canal expansion at all IOP levels. Scatterplots of ONH posterior displacement and canal expansion are shown in (**C**) and (**D**) at 10 and 30 mm Hg, respectively.

10 to 30 mm Hg. During IOP increase, the canal expansion leveled off much faster than the ONH posterior displacement.

- Within the ONH, larger strains were found in the anterior region, where the LC is located in porcine eyes. Through-thickness compression was the dominant mode of deformation, but the in-plane stretch and shear strain were also higher in the anterior ONH.
- The largest strains overall were concentrated in the periphery of the anterior ONH in the vicinity of the peripheral LC. In-plane stretch and shear strain were larger in the periphery than the center, and the shear strain showed the greatest difference between the two regions.

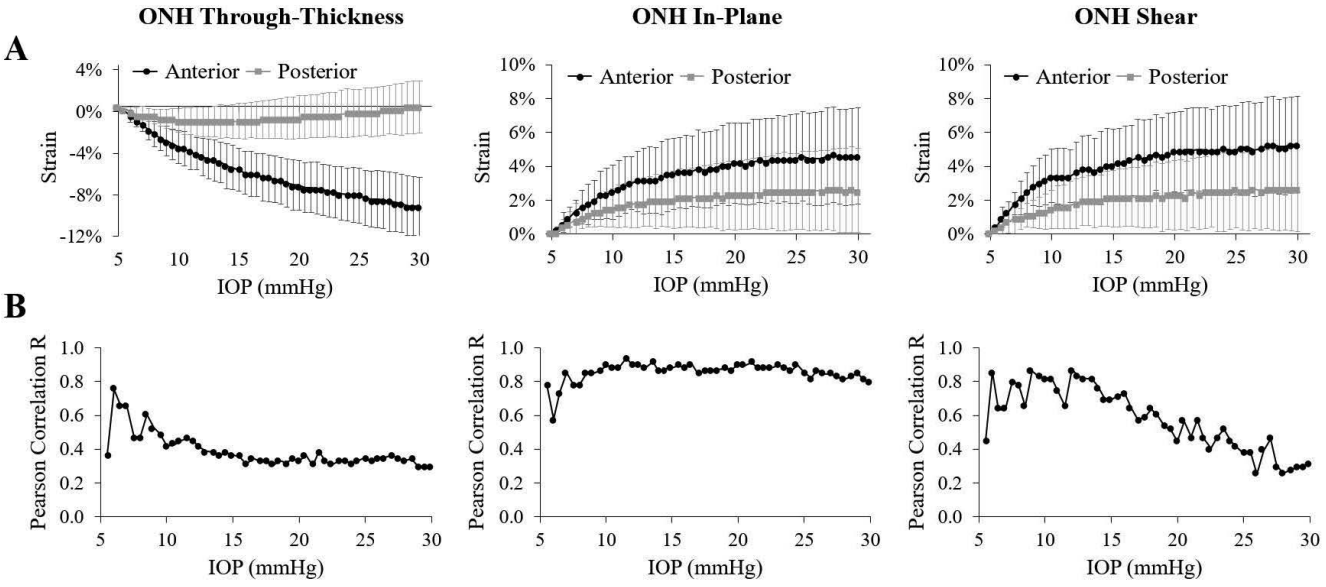

Figure 7. (**A**) Average strains in the anterior and posterior ONH during inflation ($n = 12$). (**B**) Pearson correlation between the strains in the anterior and posterior ONH at all IOP levels.

Table 1. Average Strains in the Anterior and Posterior ONH of All Eyes at 30 mm Hg ($n = 12$)

Strain (at 30 mm Hg)	Minimum, %	Maximum, %	Mean ± SD, %
Anterior ONH			
Through-Thickness	−14.55	−5.09	−9.62 ± 2.83
In-Plane	1.56	7.25	4.62 ± 1.89
Shear (magnitude)	2.23	8.09	5.30 ± 1.71
Posterior ONH			
Through-Thickness	−4.70	3.51	−0.05 ± 2.48
In-Plane	0.30	4.18	2.59 ± 1.02
Shear (magnitude)	1.43	4.43	2.63 ± 0.97

Table 2. Average Strains in the Center and Periphery of the Anterior ONH of All Eyes at 30 mm Hg ($n = 12$)

Strain (at 30 mm Hg)	Minimum, %	Maximum, %	Mean ± SD, %
Central Anterior ONH			
Through-Thickness	−14.17	−3.97	−8.70 ± 3.07
In-Plane	0.19	4.36	2.85 ± 1.23
Shear (magnitude)	1.49	5.33	3.09 ± 1.16
Peripheral Anterior ONH			
Through-Thickness	−14.78	−5.89	−10.21 ± 2.74
In-Plane	1.94	9.14	5.76 ± 2.44
Shear (magnitude)	2.61	10.64	6.69 ± 2.34

In this study, we quantified the posterior displacement of the porcine ONH and PPS, which showed a nonlinear relationship to IOP (Fig. 5A). Posterior displacement of the porcine LC and/or PPS has been reported by others using alternative imaging techniques. Coudrillier et al.[9] observed posterior displacements over nearly the same IOP range (6–30 mm Hg) by using phase-contrast μCT imaging, although quantitative analyses of the displacements were not reported. Spectral-domain OCT has been used to image the porcine ONH during increases in IOP, and a similar finding of posterior LC displacement was reported.[20] The OCT technique, however, could not measure the displacements in the sclera and the tissues posterior to the LC due to limited tissue penetration. Our ultrasound speckle tracking approach is applicable to the full thickness of both the sclera and the ONH. In addition, by performing speckle tracking on the densely sampled radiofrequency signal, we are able to achieve high sensitivity and accuracy in measuring displacements.[12,21]

With the advantages of high-frequency ultrasound speckle tracking, we were able to compare the posterior displacement of the ONH and the PPS. Although there was a strong correlation between PPS and ONH posterior displacement, the ONH consistently displaced more posteriorly than the PPS in response to acute IOP increase. To ensure that the larger ONH displacement was not simply a result of the ONH being positioned at the apex of the imaged area of the globe, we calculated the displacements in the through-thickness (i.e., radial) direction by using coordinate transformation and found a similar difference between those two regions. For example, at 30 mm Hg, the outward through-thickness displacement of the ONH was significantly larger than that of the PPS (343.7 ± 79.0 μm vs. 202.8 ± 56.8 μm; $P < 0.001$). This suggests that the larger posterior/outward displacement of the ONH may be explained by the ONH being a "weaker" discontinuity in the ocular shell surrounded by a tougher collagenous sclera. The difference in posterior movement between the ONH and PPS increased as IOP increased, likely due to IOP-related stiffening of the PPS.[22] This mismatch in posterior displacement also leads to bending deformations within ONH, especially in the peripheral ONH (see more detailed discussion later), which could potentially contribute to glaucomatous damage.

Our results showed that the porcine ONH experienced canal expansion that was smaller in magnitude than the posterior displacement (Fig. 6A). Canal expansion has been observed during porcine eye inflation,[23] and studies using digital image correlation to track the outer surface of the bovine and murine posterior sclera have also reported canal expansion that was minimal relative to posterior movement of the ONH.[24,25] This response, and the decrease in correlation between canal expansion and posterior displacement of the ONH at higher IOP, are likely attributed to the collagen annular ring within the PPS[26,27] that limits canal expansion but is less

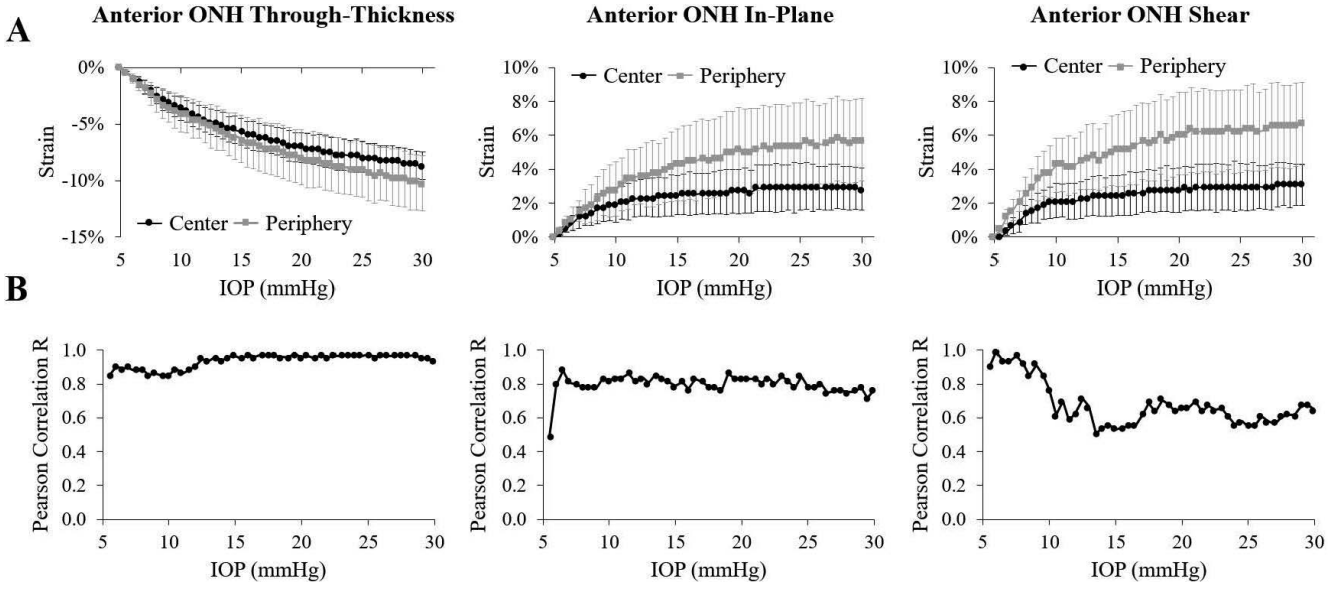

Figure 8. (**A**) Average strains in the central and peripheral regions of the anterior ONH during inflation ($n = 12$). (**B**) Pearson correlation between the central and peripheral strains at all IOP levels.

Investigative Ophthalmology & Visual Science

effective in preventing posterior displacement of the ONH.[28] This displacement pattern suggests that at higher IOP levels, the ONH bows more posteriorly with respect to the PPS, consistent with the clinical observation of ONH "cupping".[29] It has been postulated that a low sclera modulus may cause large canal expansion and anterior movement of the LC as it is pulled taut by the sclera,[30] and several computational models have predicted this behavior.[31–33] Our experimental data showed only posterior displacement of the entire ONH in response to acute IOP increase, despite the level of canal expansion. This may be explained by the overall high compliance of both the porcine LC and sclera,[34–36] which could result in both canal expansion and posterior LC displacement.[31] Future studies will investigate this behavior in human donor eyes.

Compression, stretch, and shear strains within the ONH increased nonlinearly with IOP increase. The nonlinear behavior is expected for collagenous tissues such as the sclera and cornea, but the ONH has a complex structure with a significant presence of neuroglial tissue and its nonlinear response has not been well established. Regional analyses revealed that the largest deformations occurred in the anterior ONH (Fig. 7A), and the through-thickness compression was nearly twice as large as the in-plane stretch and shear strain in this region. The LC was located within the anterior region, and, thus, the deformation measured in the anterior ONH was likely the combined response of the LC beams and intralaminar neural tissue. Our results suggest that the porcine LC experiences more through-thickness compression than in-plane stretch or shear when IOP is elevated. This is consistent with phase-contrast μCT measurements.[9] Large compressive strains have also been predicted from computational models of the human eye.[37,38] Interestingly, a recent study using scanning laser multiphoton microscopy showed essentially no anterior-posterior strain within the murine ONH.[39] This discrepancy is possibly related to differences in LC composition and structure (e.g., cellular vs. collagenous). Excessive compression of the ONH has been suggested to precede visual field defects[1] and likely contributes to axonal damage and abnormal extracellular matrix remodeling within the LC.[29] The compressive strains measured in this study were found almost exclusively within the anterior ONH where the porcine LC resides, suggesting a potential role for the LC to shield the retrolaminar tissue from compression.

Our experimental data support computational modeling predictions by Grytz et al.[28] that the ONH is largely shielded from in-plane stretch by the collagen annulus in the PPS. However, the collagen annulus is not effective in preventing compression or bending within the ONH. Significant shear was measured in the porcine ONH, especially in the periphery of the anterior ONH where the LC meets the PPS (Fig. 8A). These deformations may be a result of the mismatch in the mechanical stiffness of the PPS and ONH, because the stiffer PPS can better resist deformation while the ONH is pushed posteriorly during increases in IOP.[28] A recent study in human donor eyes also found larger maximum shear strains in the periphery of the LC.[40] The larger deformation of the peripheral LC may be partially explained by a decreased connective tissue density in this region and reflected in the earlier loss of peripheral vision in glaucoma.[41,42] These deformations may also impair capillary blood flow within the LC beams[43,44] and drive posterior migration of the LC insertion.[45,46]

This study has several limitations. First, ex vivo testing has important differences from in vivo, including the absence of retrolaminar tissue pressure and cerebrospinal fluid pressure in the subarachnoid space. These pressures may reduce posterior displacement and bending of the ONH by opposing IOP from the posterior side of the LC. Future studies are needed to evaluate the effect of these pressures on ONH displacements and strains.[47] Postmortem tissue changes may also have had some effects on our measurements. For example, positive through-thickness strains were detected in the posterior ONH in some eyes, which might be due to swelling or changes in tissue permeability.[48,49] Lower-frequency ultrasound may be used to evaluate the ONH and PPS in vivo,[50–52] but future studies are needed to optimize tissue penetration and resolution. Another limitation was that scleral strain was not computed due to there being an insufficient number of kernels for least squares strain estimation with current data acquisition methods. The optic nerve sheath may have created acoustic shadowing in the transition zone between the ONH and PPS. Strains calculations were omitted for this region and thus were not included in the ONH strain analyses (Fig. 4B). The ultrasound system used in this study also had asymmetric pixel resolution with a higher resolution in the axial (i.e., sound propagation) direction, as generally seen in all ultrasound imaging. Despite this fact, we have shown that our imaging system and speckle tracking algorithm can accurately measure strains as small as 0.025% in both the vertical and horizontal directions,[14] much smaller than the strains seen in this study. Lastly, the reliability of 2D speckle tracking is susceptible to out-of-plane tissue motion. When significant out-of-plane motion occurs, the correlation coefficient becomes lower due to substantial changes in speckle patterns. We have filtered kernels with correlation coefficients less than 0.8 to reduce the effects of potentially erroneous displacements from poor tracking. Our previous studies have shown that speckle tracking can be successfully performed with an out-of-plane displacement within 25 μm.[14] With the small incremental pressure steps (0.5 mm Hg) used in this study, the out-of-plane motion was typically well within the trackable range, as indicated by the typical high correlation coefficients (> 0.9) in a majority of kernels. 2D measurements also cannot fully describe the response of the entire ONH and PPS, and the mechanical response may differ for other cross-sections.[39] A more complete characterization will be pursued in future studies by using 3D ultrasound scans.

In summary, high-frequency ultrasound speckle tracking is a unique and powerful tool for measuring the mechanical behavior of both the ONH and PPS through the entire thickness of the tissues. The regional patterns and differences in displacements and strains observed in this study may provide important insights into the role of ONH and PPS biomechanics in the disease process of glaucoma.

Acknowledgments

Supported by National Institutes of Health grant RO1EY020929.

Disclosure: **E. Pavlatos**, None; **Y. Ma**, None; **K. Clayson**, None; **X. Pan**, None; **J. Liu**, None

References

1. Quigley HA, Hohman RM, Addicks EM, Massof RW, Green WR. Morphologic changes in the lamina cribrosa correlated with neural loss in open-angle glaucoma. *Am J Ophthalmol*. 1983; 95:673–691.
2. Elkington AR, Inman CB, Steart PV, Weller RO. The structure of the lamina cribrosa of the human eye: an immunocytochemical and electron microscopical study. *Eye*. 1990;4:42–57.
3. Burgoyne CF, Downs JC, Bellezza AJ, Francis Suh J, Hart RT. The optic nerve head as a biomechanical structure: a new paradigm for understanding the role of IOP-related stress and strain in the pathophysiology of glaucomatous optic nerve head damage. *Prog Retin Eye Res*. 2005;24:39–73.

4. Pavlatos E, Perez BC, Morris HJ, et al. Three-dimensional strains in human posterior sclera using ultrasound speckle tracking. *J Biomech Eng*. 2016;138:0210151.
5. Choi HJ, Sun D, Jakobs TC. Astrocytes in the optic nerve head express putative mechanosensitive channels. *Mol Vis*. 2015; 21:749–766.
6. Downs JC, Roberts MD, Sigal IA. Glaucomatous cupping of the lamina cribrosa: A review of the evidence for active progressive remodeling as a mechanism. *Exp Eye Res*. 2011; 93:133–140.
7. Mari JM, Strouthidis NG, Park SC, Girard MJA. Enhancement of lamina cribrosa visibility in optical coherence tomography images using adaptive compensation. *Invest Ophthalmol Vis Sci*. 2013;54:2238–2247.
8. Sigal IA, Grimm JL, Jan N, Reid K, Minckler DS, Brown DJ. Eye-specific IOP-induced displacements and deformations of human lamina cribrosa. *Invest Ophthalmol Vis Sci*. 2014;55: 1–15.
9. Coudrillier B, Geraldes DM, Vo NT, et al. Phase-contrast micro-computed tomography measurements of the intraocular pressure-induced deformation of the porcine lamina cribrosa. *IEEE Trans Med Imaging*. 2016;35:988–999.
10. Sigal IA, Flanagan JG, Tertinegg I, Ethier CR. Finite element modeling of optic nerve head biomechanics. *Invest Ophthalmol Vis Sci*. 2004;45:4378–4387.
11. Norman RE, Flanagan JG, Sigal IA, Rausch SMK, Tertinegg I, Ethier CR. Finite element modeling of the human sclera: Influence on optic nerve head biomechanics and connections with glaucoma. *Exp Eye Res*. 2011;93:4–12.
12. Tang J, Liu J. Ultrasonic measurement of scleral cross-sectional strains during elevations of intraocular pressure: method validation and initial results in posterior porcine sclera. *J Biomech Eng*. 2012;134:091007.
13. Palko JR, Tang J, Cruz Perez B, Pan X, Liu J. Spatially heterogeneous corneal mechanical responses before and after riboflavin–ultraviolet-A crosslinking. *J Cataract Refract Surg*. 2014;40:1021–1031.
14. Pavlatos E, Chen H, Clayson K, Pan X, Liu J. Imaging corneal biomechanical responses to ocular pulse using high-frequency ultrasound. *IEEE Trans Med Imaging*. 2018;37:663–670.
15. Kallel F, Ophir J. A least-squares strain estimator for elastography. *Ultrason Imaging*. 1997;19:195–208.
16. Huang Y, Hsu JC. Hochberg's step-up method: cutting corners off holm's step-down method. *Biometrika*. 2007;94:965–975.
17. Fatehee N, Yu PK, Morgan WH, Cringle SJ, Yu D. Correlating morphometric parameters of the porcine optic nerve head in spectral domain optical coherence tomography with histological sections. *Br J Ophthalmol*. 2011;95:585–589.
18. Pastor-Idoate S, Bonshek R, Irion L, et al. Ultrastructural and histopathologic findings after pars plana vitrectomy with a new hypersonic vitrector system. Qualitative preliminary assessment. *PLoS One*. 2017;12:e0173883.
19. Chien JL, Ghassibi MP, Mahadeshwar P, et al. A novel method for assessing lamina cribrosa structure ex vivo using anterior segment enhanced depth imaging optical coherence tomography. *J Glaucoma*. 2017;26:626–632.
20. Fatehee N, Yu PK, Morgan WH, Cringle SJ, Yu D. The impact of acutely elevated intraocular pressure on the porcine optic nerve head. *Invest Ophthalmol Vis Sci*. 2011;52:6192–6198.
21. Cruz Perez B, Pavlatos E, Morris H, et al. Mapping 3D strains with ultrasound speckle tracking: method validation and initial results in porcine scleral inflation. *Ann Biomed Eng*. 2016;44:2302–2312.
22. Thornton IL, Dupps WJ, Roy AS, Krueger RR. Biomechanical effects of intraocular pressure elevation on optic nerve/lamina cribrosa before and after peripapillary scleral collagen cross-linking. *Invest Ophthalmol Vis Sci*. 2009;50:1227–1233.
23. Girard MJA, Downs JC, Burgoyne CF, Suh JF. Experimental surface strain mapping of porcine peripapillary sclera due to elevations of intraocular pressure. *J Biomech Eng*. 2008;130: 041017.
24. Myers KM, Coudrillier B, Boyce BL, Nguyen TD. The inflation response of the posterior bovine sclera. *Acta Biomaterialia*. 2010;6:4327–4335.
25. Myers KM, Cone FE, Quigley HA, Gelman S, Pease ME, Nguyen TD. The in vitro inflation response of mouse sclera. *Exp Eye Res*. 2010;91:866–875.
26. Pijanka JK, Spang MT, Sorensen T, et al. Depth-dependent changes in collagen organization in the human peripapillary sclera. *PLoS One*. 2015;10:e0118648.
27. Jones HJ, Girard MJ, White N, et al. Quantitative analysis of three-dimensional fibrillar collagen microstructure within the normal, aged and glaucomatous human optic nerve head. *J R Soc Interface*. 2015;12:20150066.
28. Grytz R, Meschke G, Jonas J. The collagen fibril architecture in the lamina cribrosa and peripapillary sclera predicted by a computational remodeling approach. *Biomech Model Mechanobiol*. 2011;10:371–382.
29. Burgoyne C. The morphological difference between glaucoma and other optic neuropathies. *J Neuroophthalmol*. 2015; 35(suppl 1):8–21.
30. Sigal IA, Ethier CR. Biomechanics of the optic nerve head. *Exp Eye Res*. 2009;88:799–807.
31. Sigal IA, Yang H, Roberts MD, Burgoyne CF, Downs JC. IOP-induced lamina cribrosa displacement and scleral canal expansion: an analysis of factor interactions using parameterized eye-specific models. *Invest Ophthalmol Vis Sci*. 2011;52: 1896–1907.
32. Sigal IA, Yang H, Roberts MD, et al. IOP-induced lamina cribrosa deformation and scleral canal expansion: independent or related? *Invest Ophthalmol Vis Sci*. 2011;52:9023–9032.
33. Roberts MD, Liang Y, Sigal IA, et al. Correlation between local stress and strain and lamina cribrosa connective tissue volume fraction in normal monkey eyes. *Invest Ophthalmol Vis Sci*. 2010;51:295–307.
34. Wollensak G, Spoerl E. Collagen crosslinking of human and porcine sclera. *J Cataract Refract Surg*. 2004;30:689–695.
35. Schultz DS, Lotz JC, Lee SM, Trinidad ML, Stewart JM. Structural factors that mediate scleral stiffness. *Invest Ophthalmol Vis Sci*. 2008;49:4232–4236.
36. Cruz-Perez B, Tang J, Morris HJ, et al. Biaxial mechanical testing of posterior sclera using high-resolution ultrasound speckle tracking for strain measurements. *J Biomech*. 2014; 47:1151–1156.
37. Sigal IA, Flanagan JG, Tertinegg I, Ethier CR. Predicted extension, compression and shearing of optic nerve head tissues. *Exp Eye Res*. 2007;85:312–322.
38. Sigal IA, Flanagan JG, Tertinegg I, Ethier CR. Modeling individual-specific human optic nerve head biomechanics. Part I: IOP-induced deformations and influence of geometry. *Biomech Model Mechanobiol*. 2009;8:85–98.
39. Nguyen C, Midgett D, Kimball EC, et al. Measuring deformation in the mouse optic nerve head and peripapillary sclera. *Invest Ophthalmol Vis Sci*. 2017;58:721–733.
40. Midgett DE, Pease ME, Jefferys JL, et al. The pressure-induced deformation response of the human lamina cribrosa: analysis of regional variations. *Acta Biomaterialia*. 2017;53:123–139.
41. Quigley HA, Addicks EM. Regional differences in the structure of the lamina cribrosa and their relation to glaucomatous optic nerve damage. *Arch Ophthalmol*. 1981;99:137–143.
42. Dandona L, Quigley HA, Brown AE, Enger C. Quantitative regional structure of the normal human lamina cribrosa. A racial comparison. *Arch Ophthalmol*. 1990;108:393–398.

Investigative Ophthalmology & Visual Science

43. Tektas O, Lütjen-Drecoll E, Scholz M. Qualitative and quantitative morphologic changes in the vasculature and extracellular matrix of the prelaminar optic nerve head in eyes with POAG. *Invest Ophthalmol Vis Sci*. 2010;51:5083–5091.
44. Jonas JB, Jonas SB. Histomorphometry of the circular peripapillary arterial ring of Zinn-Haller in normal eyes and eyes with secondary angle-closure glaucoma. *Acta Ophthalmol*. 2010;88:317–322.
45. Yang H, Williams G, Downs JC, et al. Posterior (outward) migration of the lamina cribrosa and early cupping in monkey experimental glaucoma. *Invest Ophthalmol Vis Sci*. 2011;52:7109–7121.
46. Sigal IA, Flanagan JG, Lathrop KL, Tertinegg I, Bilonick R. Human lamina cribrosa insertion and age. *Invest Ophthalmol Vis Sci*. 2012;53:6870–6879.
47. Feola AJ, Coudrillier B, Mulvihill JJ, et al. Deformation of the lamina cribrosa and optic nerve due to changes in cerebrospinal fluid pressure. *Invest Ophthalmol Vis Sci*. 2017;58:2070–2078.
48. Flage T. Permeability properties of the tissues in the optic nerve head region in the rabbit and the monkey. *Acta Ophthalmologica*. 1977;55:652–664.
49. Ayyalasomayajula A, Park RI, Simon BR, Vande Geest JP. A porohyperelastic finite element model of the eye: the influence of stiffness and permeability on intraocular pressure and optic nerve head biomechanics. *Comput Methods Biomech Biomed Engin*. 2016;19:591–602.
50. Dikici AS, Mihmanli I, Kilic F, et al. In vivo evaluation of the biomechanical properties of optic nerve and peripapillary structures by ultrasonic shear wave elastography in glaucoma. *Iran J Radiol*. 2016;13:e36849.
51. Agladioglu K, Pekel G, Kasikci SA, Yagci R, Kiroglu Y. An evaluation of ocular elasticity using real-time ultrasound elastography in primary open-angle glaucoma. *Br J Radiol*. 2016;89:20150429.
52. Unal O, Cay N, Yulek F, Taslipinar AG, Bozkurt S, Gumus M. Real-time ultrasound elastographic features of primary open angle glaucoma. *Ultrasound Q*. 2016;32:333–337.

Investigative Ophthalmology & Visual Science